Evidence for Climate Change in the Satellite Cloud Record

Authors: Joel R. Norris[1]*, Robert J. Allen[2], Amato T. Evan[1], Mark D. Zelinka[3], Christopher W. O'Dell[4], and Stephen A. Klein[3]

Affiliations: [1]Scripps Institution of Oceanography, University of California at San Diego, La Jolla, California

[2]Department of Earth Sciences, University of California at Riverside, Riverside, California

[3]Program for Climate Model Diagnosis and Intercomparison, Lawrence Livermore National Laboratory, Livermore, California

[4]Cooperative Institute for Research in the Atmosphere, Colorado State University, Fort Collins, Colorado

*Correspondence to: jnorris@ucsd.edu

Clouds substantially impact Earth's energy budget by reflecting solar radiation back to space and by restricting emission of thermal radiation to space[1]. They are perhaps the largest uncertainty in our understanding of climate change due to disagreement among climate models and observational datasets over what cloud changes have occurred during recent decades and will occur in response to global warming[2,3]. This is because observational systems originally designed for monitoring weather have lacked sufficient stability to reliably detect cloud changes over decades unless they have been corrected to

remove spurious artifacts[4,5]. Here we show that several independent corrected satellite records exhibit large-scale patterns of cloud change between the 1980s and 2000s that are similar to those produced by model simulations of climate with recent historical external radiative forcing. Observed and simulated cloud change patterns are consistent with poleward retreat of midlatitude storm tracks, expansion of subtropical dry zones, and increasing height of the highest cloud tops at all latitudes. The primary drivers of these cloud changes appear to be increasing greenhouse gas concentrations and a recovery from volcanic radiative cooling. These results indicate that the cloud changes most consistently predicted by global climate models are currently occurring in nature.

The International Satellite Cloud Climatology Project (ISCCP) dataset and the Pathfinder Atmospheres - Extended (PATMOS-x) dataset are the two longest satellite records of cloudiness[6,7]. The datasets consist of cloud retrievals made by multiple weather satellites over several decades, and in their original form, the long-term records suffer from spurious variability related to changes in satellite orbit, instrument calibration, and other factors[4,5,8]. Previous studies using these datasets to investigate the cloud response to global warming have obtained inconclusive results due to the dominating presence of artifacts[9,10,11]. Here we use corrected versions of ISCCP and PATMOS-x from which spurious variability has been removed[5]. The correction procedure unfortunately also removes any real cloud variability at near-global scales, thus precluding examination of global mean cloud changes. Instead, we examine large-scale patterns of observed cloud change for consistency with patterns projected by global climate models to occur with climate change[10,12]. For corroboration of the corrected ISCCP and PATMOS-x records, we additionally investigate the change in albedo from the 1980s Earth Radiation Budget Satellite (ERBS)[13] to the 2000s Clouds and the Earth's Radiant Energy System

(CERES) satellite instruments[14,15] and changes in ocean-only liquid water path from the Multi-Sensor Advanced Climatology of Liquid Water Path (MAC-LWP) dataset[16].

Figure 1a displays the spatial distribution of trends during 1983-2009 for averaged ISCCP and PATMOS-x total cloud amount, and Figure 1b displays the spatial distribution of differences between 2002-2014 CERES albedo and 1985-1989 ERBS albedo. All observational records agree that cloud amount and albedo increased over the northwest Indian Ocean, the northwest and southwest tropical Pacific, and north of the equator in the Pacific and Atlantic. Cloud amount and albedo decreased over midlatitude oceans in both hemispheres (especially the North Atlantic), over the southeast Indian Ocean, and in a northwest-to-southeast line stretching across the central tropical South Pacific. MAC-LWP exhibits a similar trend pattern in liquid water path during 1988-2014 (Extended Data Fig. 1a). Shifting the start or end time of trend calculation by several years has little impact on the spatial pattern of change. Similar patterns occur for differences in total cloud amount and albedo between 1985-1989 and 2003-2009, the time periods during which ISCCP, PATMOS-x, and ERBS/CERES completely overlap (Extended Data Fig. 2).

Are the observed cloud changes solely a manifestation of natural internal variability or are they also a response to external radiative forcing of the climate system? We address this question by examining simulations from the Coupled Model Intercomparison Project Phase 5 (CMIP5) multi-model dataset[17]. Historical simulations included anthropogenic greenhouse gas concentrations, ozone, land use changes, anthropogenic aerosols, volcanic aerosols, and solar output and thus represent our best estimate of the climate response to recent external radiative forcing (Extended Data Table 1). Figure 1c displays the spatial distribution of trends in ensemble mean modeled total cloud amount during the 27-year period 1983-2009 for all radiative forcings

(ALL). Observations and models exhibit widespread agreement on which areas have increasing and decreasing cloud amount (Fig. 1d). Table 1 lists the spatial correlation between observed and simulated cloud trends.

Could natural internal variability alone produce the correlation between the observed and simulated cloud trend patterns? We assess the likelihood of this outcome by examining cloud trends during 27-year periods from CMIP5 preindustrial (PI) simulations without external radiative forcing (Extended Data Table 2). Calculating the spatial correlation between the ensemble mean ALL trend pattern and the trend pattern of each 27-year PI period generates a probability distribution of correlation values arising purely from natural internal variability (Extended Data Fig. 3). We find that no 27-year period in more than 15000 years of PI simulations exhibits a correlation coefficient as positive as that between the observed and ensemble mean ALL trend patterns, suggesting that external radiative forcing was a driving factor in large-scale cloud changes from the 1980s to the 2000s.

One prominent feature of Fig. 1 and robust prediction by climate models is the widespread reduction in cloudiness at middle latitudes[2,10,12,18]. Figures 2a and 2b show trends in zonal mean total cloud amount during 1983-2009 for ISCCP and PATMOS-x, and Fig. 2c shows zonal mean differences between 2002-2014 CERES albedo and 1985-1989 ERBS albedo. Every observational record exhibits a decline in cloud amount or albedo at middle latitudes in both hemispheres that is nearly always statistically significant. The ocean-only MAC-LWP dataset also reports less liquid water path around 40° (Extended Data Fig. 1b). Previous research found evidence for tropical expansion in recent decades[19.] Reduced cloudiness around 40° is consistent with a poleward expansion of the subtropical dry zone cloud minimum and poleward retreat of the storm track cloud maximum.

Figure 2d displays trends in zonal mean total cloud amount during 1983-2009 from the ALL simulations. Most individual simulations exhibit reduced cloud amount at middle latitudes of both hemispheres, and the ensemble mean trends are statistically significant. Furthermore, the majority of simulations reproduce the observed increase in cloud amount and albedo occurring in the northern tropics. The spatial correlation between observed and simulated zonal cloud trends is highly significant (Table 1 and Extended Data Fig. 3).

Since the correction procedures applied to the satellite datasets removed any real global mean change that might be present, for maximum comparability we subtracted the 60°S-60°N average change in total cloud amount from the model output prior to creating Figs. 1c, 1d, and 2d. Without this adjustment, ALL ensemble mean cloud amount averaged over 60°S-60°N decreases by 0.13 %-cloud-amount over 25 years. Although highly statistically significant, the modeled reduction in 60°S-60°N average cloud amount during 1983-2009 is far smaller than what is detectable by our observational systems. Extended Data Figs. 4a and 4b show ALL cloud trends without the subtraction of the 60°S-60°N average change. They exhibit patterns similar to those seen in Figs. 1c and 2d.

Another robust prediction by climate models is rising height of high cloud tops at all latitudes[10,12,18,20]. Figure 3a displays ISCCP climatological zonal mean cloud amount within 7 cloud top pressure intervals. Only amounts of clouds with optical thickness greater than 3.6 are plotted to reduce uncertainty in cloud top pressure retrievals. A local maximum in cloud amount occurs in the 180-310 hPa interval in the tropics whereas clouds are typically no higher than 310 hPa in the midlatitude storm tracks, following the latitudinal variation of tropopause height. Figures 3b and 3c show that ISCCP and PATMOS-x zonal mean cloud amount increased in the 50-180 hPa interval and decreased in the 180-310 hPa interval during 1983-2009 in the tropics, consistent with a rise in the tops of the highest clouds. The cloud amount increase in the 180-310 hPa interval at middle latitudes similarly suggests a rise in the highest cloud tops.

Figure 3d displays trends in zonal mean cloud amount during 1983-2009 from the ALL ensemble mean. The pattern of modeled cloud trends is highly correlated with the satellite record in the 50-180 hPa and 180-310 hPa intervals, suggesting the observed rise in cloud top is at least partly due to external radiative forcing. We expect less agreement below these levels because the ISCCP and PATMOS-x satellite retrievals cannot detect lower clouds underneath higher clouds whereas the models report the exact cloud amount at each level. Note that the negative trends in cloud amount occurring in the 50-180 hPa interval at higher latitudes are relative to the 60°S-60°N average cloud change for that interval and do not correspond to an actual reduction in cloudiness. Extended Data Fig. 4c, for which the 60°S-60°N average change was not subtracted, shows that modeled cloud amount in the 50-180 hPa interval merely increases less at higher latitudes than at lower latitudes.

What specific factors are contributing to the observed cloud changes? We address this question by examining additional CMIP5 simulations listed in Extended Data Table 1 with external radiative forcing only from greenhouse gases (GHG), only from anthropogenic aerosol (AA), only from ozone (OZ), and only from natural solar variations and volcanic aerosol (NAT). Extended Data Figs. 5, 6, and 7 display the ensemble mean modeled cloud trends for GHG, AA, OZ, and NAT simulations. The GHG and NAT simulations both produce modeled cloud trend patterns that are significantly correlated with the observed cloud trend pattern (Table 1 and Extended Data Fig. 3). This includes decreasing total cloud amount at middle latitudes (GHG and NAT), increasing total cloud amount in the northern tropics (NAT), and increasing cloud amount in the 50-180 hPa interval in the tropics and in the 180-310 hPa interval at middle latitudes (GHG and NAT). Contrastingly, the AA and OZ simulations do not produce cloud trends that globally resemble the observed cloud trends, as demonstrated by insufficiently positive correlation (Table 1). The OZ simulations do exhibit reduced cloud amount at southern hemisphere middle latitudes[21].

Both GHG and NAT simulations experience increasing tropospheric temperature and decreasing stratospheric temperature from the 1980s and the 2000s. This is caused by increasing greenhouse gases in the former case and a recovery from the 1982 El Chichón and 1991 Pinatubo volcanic aerosol episodes in the latter case[22,23,24]. Tropospheric warming and stratospheric cooling promote an increase in the height of the highest cloud tops[25,26], and together with global warming, promote an expansion of the tropical zone and poleward shift of storm tracks[27,28]. Depleted stratospheric ozone is an additional factor promoting a poleward shift of the southern hemisphere storm track[21,29].

Expansion of subtropical dry zones results in less reflection of solar radiation back to space. As cloud tops rise, their greenhouse effect becomes stronger. Both of these cloud changes have a warming effect on climate. Our results suggest that radiative forcing by a combination of anthropogenic greenhouse gases and volcanic aerosol has produced observed cloud changes during the past several decades that exert positive feedbacks on the climate system. We expect increasing greenhouse gases will cause these cloud trends to continue in the future unless offset by unpredictable large volcanic eruptions.

References

1. Ramanathan, V. *et al.* Cloud-radiative forcing and climate: results from the Earth Radiation Budget Experiment. *Science*, **243**, 57-63 (1989).

2. Boucher, O. *et al.* In *Climate Change 2013: The Physical Science Basis. Contribution of* Working *Group I to the Fifth Assessment Report of the Intergovernmental Panel on Climate Change* (eds. Stocker, T. F. *et al.*) Ch. 7, 571-657 (Cambridge University Press, 2013).

3. Dufresne, J.-L., & Bony, S. An assessment of the primary sources of spread of global warming estimates from coupled atmosphere–ocean models. *J. Climate*, **21**, 5135–5144 (2008).

4. Evan, A. T., Heidinger, A. K., & Vimont, D. J. Arguments against a physical long-term trend in global ISCCP cloud amounts. *Geophys. Res. Lett.*, **34**, L04701, doi:10.1029/2006GL028083 (2007).

5. Norris, J. R., & Evan, A. T. Empirical removal of artifacts from the ISCCP and PATMOS-x satellite cloud records. *J. Atmos. Oceanic Tech.*, **32**, 691–702 (2015).

6. Rossow, W. B., & Schiffer, R. A. Advances in understanding clouds from ISCCP. *Bull. Amer. Meteor. Soc.*, **80**, 2261- 2287 (1999).

7. Heidinger, A. K., Foster, M. J., Walther, A., & Zhao, Z. The Pathfinder Atmospheres Extended (PATMOS-x) AVHRR climate data set. *Bull. Amer. Meteor. Soc.*, **95**, 909–922 (2014).

8. Marchand, R, Trends in ISCCP, MISR, and MODIS cloud-top-height and optical-depth histograms, *J. Geophys. Res.*, **118**, 1941–1949 (2013).

9. Bender, F. A.-M., Ramanathan, V., & Tselioudis, G. Changes in extratropical storm track cloudiness 1983-2008: Observational support for a poleward shift, *Clim. Dyn.*, **38**, 2037-2053 (2012).

10. Marvel, K. *et al.* External influences on modeled and observed cloud trends. *J. Climate,* **28**, 4820-4840 (2015).

11. Eastman, R., & Warren, S. G., A 39-yr survey of cloud changes from land stations worldwide 1971–2009: Long-term trends, relation to aerosols, and expansion of the Tropical belt, *J. Climate*, **26**, 1286–1303 (2013).

12. Zelinka, M. D., Klein, S. A., & Hartmann, D. L. Computing and partitioning cloud feedbacks using cloud property histograms. Part II: Attribution changes in cloud amount, altitude, and optical depth. *J. Climate*, **25**, 3736-3754 (2012).

13. Barkstrom, B. E. *et al.* Earth Radiation Budget Experiment (ERBE) archival and April 1985 results., *Bull. Am. Meteorol. Soc.*, **70**, 1254-1262 (1989).

14. Wielicki, B. A. *et al.*, Clouds and the Earth's Radiant Energy System (CERES): an Earth observing experiment. *Bull. Am. Meteorol. Soc.*, **77**, 853-868 (1996).

15. Loeb, N. G. *et al.* Toward optimal closure of the Earth's TOA radiation budget, *J. Climate*, **22**, 748-766, (2009).

16. O'Dell, C. W., Wentz, F. J., & Bennartz, R. Cloud liquid water path from satellite-based passive microwave observations: a new climatology over the global oceans, *J. Climate,* **21**, 1721-1739 (2008).

17. Taylor, K. E., Stouffer, R. J. & Meehl, G. A. An overview of CMIP5 and the experimental design. *Bull. Amer. Meteorol. Soc.* **93**, 485-498 (2012).

18. Wetherald, R. T., & Manabe, S. Cloud feedback processes in a general circulation model. *J. Atmos. Sci.* **45**, 1397-1415 (1988).

19. Seidel, D. J., Fu, Q., Randel, W. J., & Reichler, T. J. Widening of the tropical belt in a changing climate. *Nature Geosci*., **1**, doi:10.1038/ngeo.2007.38 (2008).

20. Chepfer, H., Noel, V., Winker, D., & Chiriaco, M. Where and when will we observe cloud changes due to climate warming? *Geophys. Res. Lett.*, **41**, 8387-8395, (2014).

21. Grise, K. M., Polvani, L. M., Tselioudis, G., Wu, Y., & Zelinka, M. D. The ozone hole indirect effect: cloud-radiative anomalies accompanying the poleward shift of the eddy-driven jet in the Southern Hemisphere, *Geophys. Res. Lett.*, **40**, 3688-3692 (2013).

22. Vallis, G. K., Zurita-Gotor, P., Cairns, C. and Kidston, J. Response of the large-scale structure of the atmosphere to global warming. *Q.J.R. Meteorol. Soc.*, doi: 10.1002/qj.2456 (2014).

23. Dutton, E. G., & Christy, J. R. Solar radiative forcing at selected locations and evidence for global lower tropospheric cooling following the eruptions of El Chichón and Pinatubo. *Geophys. Res. Lett.*, **19**, 2313-2316 (1992).

24. Labitzke, K., & McCormick, M. P., Stratospheric temperature increases due to Pinatubo aerosols. *Geophys. Res. Lett.*, **19**, 207-210 (1992).

25. Hartmann, D. L., & Larson, K. An important constraint on tropical cloud-climate feedback. *Geophys. Res. Lett.*, **29**, 1951, (2002).

26. Zelinka, M.D., & Hartmann, D. L. Why is longwave cloud feedback positive? *J. Geophys. Res.*, **115**, D16117, doi:10.1029/2010JD013817 (2010).

27. Held, I. M., & Hou, A. Y. Nonlinear axially symmetric circulations in a nearly inviscid atmosphere. *J. Atmos. Sci.*, **37**, 515–533 (1980).

28. Lu, J., Vecchi, G. A., Reichler Y. Expansion of the Hadley cell under global warming, *Geophys. Res. Lett.*, **34**, L06805, (2007).

29. Polvani, L. M., Waugh, D. W., Correa, G. J. P., & Son, S. W. Stratospheric ozone depletion: the main driver of Twentieth-Century atmospheric circulation changes in the Southern Hemisphere. *J. Climate*, 24, 795–812 (2011).

Acknowledgements

NOAA awards NA10OAR4310140 and NA10OAR4310141 supported work by J. R. N. and A. T. E. The efforts of M. D. Z. and S. A. K. were supported by the U. S. Department of Energy (DOE), Office of Science, Office of Biological and Environmental Research through its Regional and Global Climate Modeling Program and were performed under the auspices of DOE by Lawrence Livermore National Laboratory under Contract DE-AC52-07NA27344. Part of the work by M. D. Z. was supported by the NASA New Investigator Program (NNH14AX83I). The MAC-LWP climatology is supported by the NASA MEaSUREs Program (NNH12ZDA001N). We acknowledge the WCRP's Working Group on Coupled Modelling, which is responsible for CMIP, and we thank the climate modelling groups for producing and making available their model output. For CMIP the U.S. DOE's Program for Climate Model Diagnosis and Intercomparison provides coordinating support and led development of software infrastructure in partnership with the Global Organization for Earth System Science Portals.

Author Contributions

J. R. N. designed the study, provided ERBS, CERES, and ISCCP data, did the main analysis, and wrote the paper; R. J. A. provided standard model cloud output for CMIP5 simulations and analyzed CMIP5 meteorological output; A. T. E. provided corrected PATMOS-x data; M. D. Z. provided CMIP5 COSP cloud output; C. W. O. provided MAC-LWP liquid water path data; S. A. K. provided background information and ideas. All authors discussed the results and commented on the manuscript.

Author Information

Corrected ISCCP and PATMOS-x cloud amount data are available from the Research Data Archive at NCAR under doi:10.5065/D62J68XR. Reprints and permissions information is available at www.nature.com/reprints. The authors declare no competing financial interests. Correspondence and requests for materials should be addressed to J. R. N. (jnorris@ucsd.edu).

Table 1

Correlation between Observed and Modeled Cloud Trend Patterns

	Forcing Type				
Spatial Pattern	ALL	GHG	AA	OZ	NAT
Grid Box Total Cloud Amount	0.39 (0.0001) [0.003]	0.21 (0.05) [0.08]	0.00	0.00	0.26 (0.03) [0.04]
Zonal Mean Total Cloud Amount	0.80 (0.002) [0.009]	0.62 (0.008) [0.06]	-0.35	0.27	0.69 (0.03) [0.03]
Zonal Mean Cloud Amount in 50-180 hPa and 180-320 hPa Intervals	0.76 (0.003) [0.03]	0.73 (0.004) [0.04]	-0.62		0.73 (0.003) [0.04]

Parentheses and square brackets indicate one-sided *p*-values obtained from PI simulations shown in Extended Data Fig. 3 and from formal significance tests, respectively

Figure Legends

Figure 1 | Change in observed and simulated cloud amount and albedo between the 1980s and 2000s. a, Linear trend in average of PATMOS-x and ISCCP total cloud amount during 1983-2009. **b,** Change in albedo from Jan 1985-Dec 1989 (ERBS) to Jul 2002-Jun 2014 (CERES). **c,** Trend in ensemble mean total cloud amount during 1983-2009 from CMIP5 historical simulations with all radiative forcings (ALL). **d,** Locations where the majority of observational datasets and majority of historical simulations show increasing (cyan) or decreasing (orange) cloud amount or albedo. Black dots indicate agreement among all three satellite records on sign of change in **a** and **b** and indicate trend statistical significance ($p < 0.05$ two-sided) in **c**. All trends and changes are relative to the 60°S-60°N mean change.

Figure 2 | Zonal mean change in observed and simulated cloud amount and albedo between the 1980s and 2000s. a, ISCCP total cloud amount during 1983-2009. **b,** PATMOS-x total cloud amount during 1983-2009. **c,** Albedo from Jan 1985-Dec 1989 (ERBS) to Jul 2002-Jun 2014 (CERES). **d,** Ensemble mean total cloud amount during 1983-2009 from CMIP5 historical simulations with all radiative forcings (ALL). Zonal mean climatology is red, linear trend or change is black, circles indicate trend statistical significance ($p < 0.05$ two-sided), and bars indicate interquartile range of individual simulations. All trends and changes are relative to the 60°S-60°N mean change.

Figure 3 | Zonal mean change in observed and simulated cloud amount during 1983-2009 in 7 pressure intervals. a, ISCCP climatological cloud amount. **b,** Trend in ISCCP cloud amount during 1983-2009. **c,** Trend in PATMOS-x cloud amount during 1983-2009. **d,** Trend in ensemble mean cloud amount during 1983-2009 from CMIP5 historical simulations with all radiative forcings (ALL). For ISCCP and PATMOS-x, only amount of clouds with optical thickness $\tau > 3.6$ is plotted. Black dots indicate trend statistical significance ($p < 0.05$ two-sided). All trends are relative to the 60°S-60°N mean trend for that pressure interval.

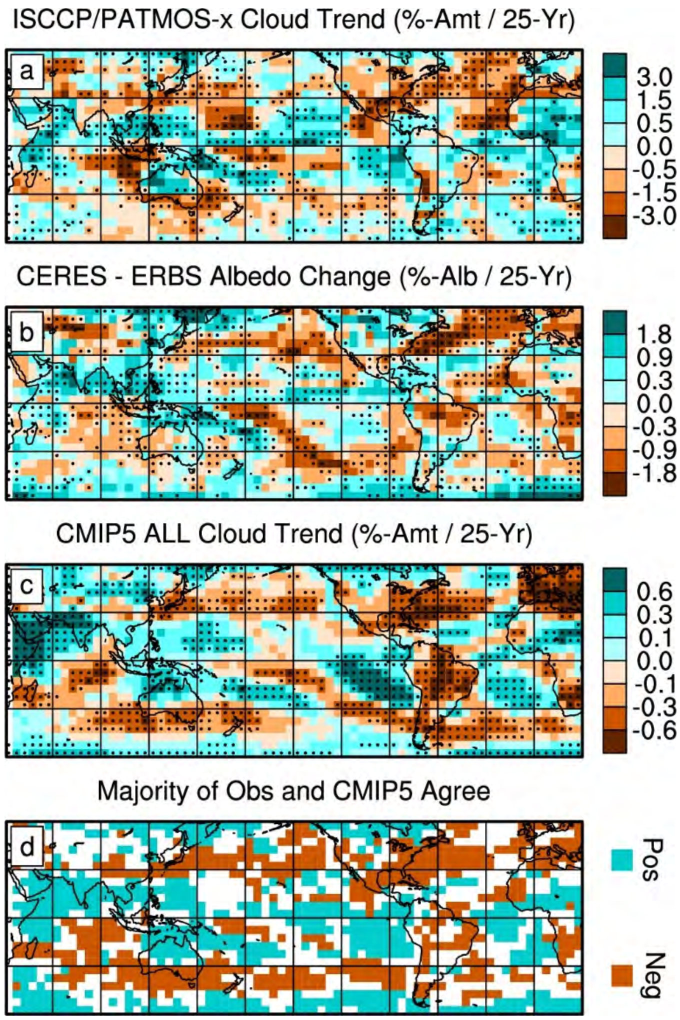

Figure 1 | Change in observed and simulated cloud amount and albedo between the 1980s and 2000s. a, Linear trend in average of PATMOS-x and ISCCP total cloud amount during 1983-2009. **b,** Change in albedo from Jan 1985-Dec 1989 (ERBS) to Jul 2002-Jun 2014 (CERES). **c,** Trend in ensemble mean total cloud amount during 1983-2009 from CMIP5 historical simulations with all radiative forcings (ALL). **d,** Locations where the majority of observational datasets and majority of historical simulations show increasing (cyan) or decreasing (orange) cloud amount or albedo. Black dots indicate agreement among all three satellite records on sign of change in **a** and **b** and indicate trend statistical significance ($p < 0.05$ two-sided) in **c**. All trends and changes are relative to the 60°S-60°N mean change.

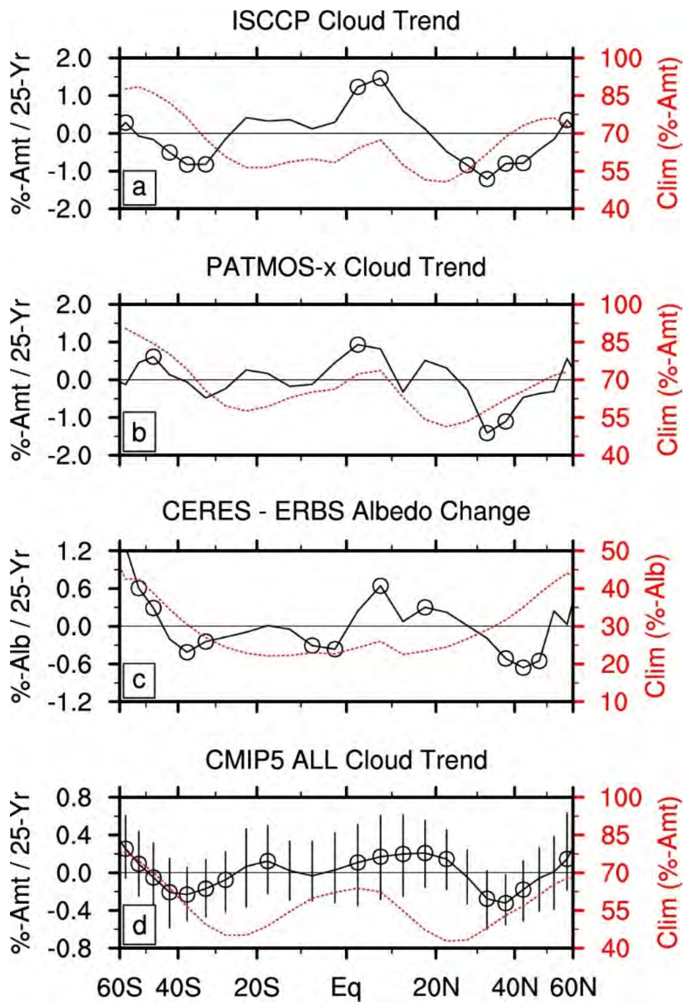

Figure 2 | Zonal mean change in observed and simulated cloud amount and albedo between the 1980s and 2000s. a, ISCCP total cloud amount during 1983-2009. **b,** PATMOS-x total cloud amount during 1983-2009. **c,** Albedo from Jan 1985-Dec 1989 (ERBS) to Jul 2002-Jun 2014 (CERES). **d,** Ensemble mean total cloud amount during 1983-2009 from CMIP5 historical simulations with all radiative forcings (ALL). Zonal mean climatology is red, linear trend or change is black, circles indicate trend statistical significance ($p < 0.05$ two-sided), and bars indicate interquartile range of individual simulations. All trends and changes are relative to the 60°S-60°N mean change.

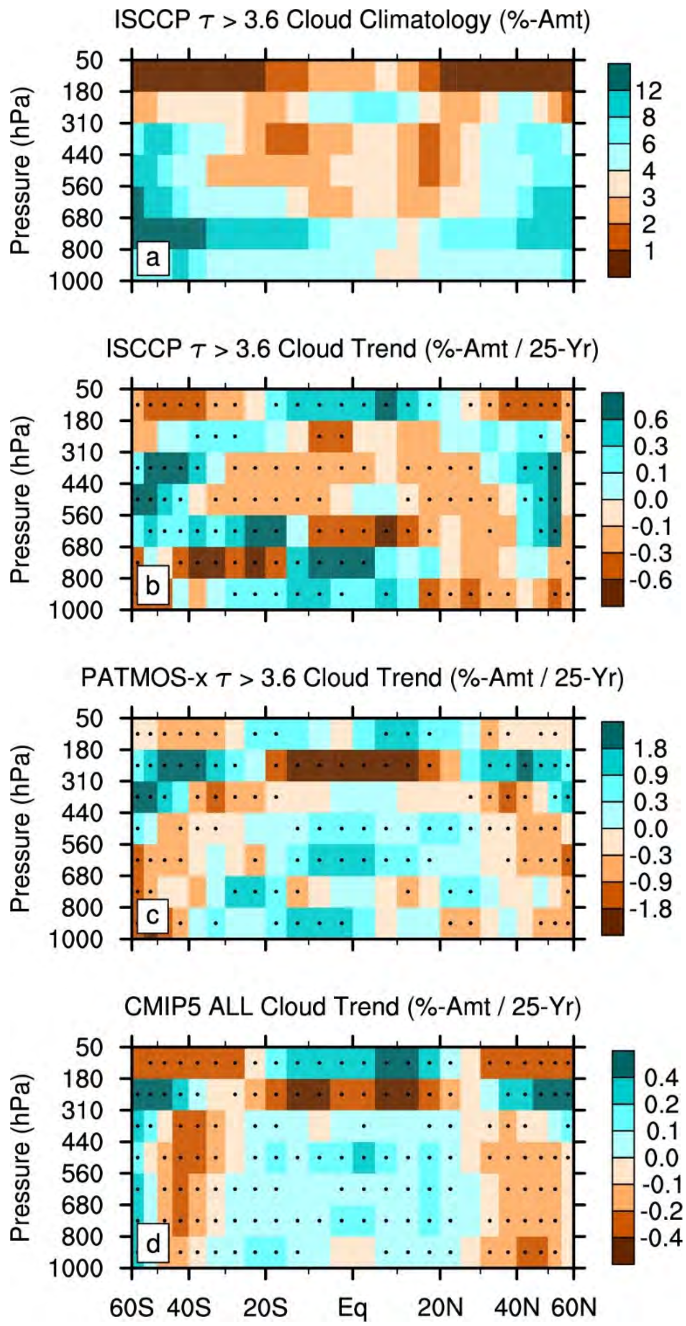

Figure 3 | Zonal mean change in observed and simulated cloud amount during 1983-2009 in 7 pressure intervals. a, ISCCP climatological cloud amount. **b,** Trend in ISCCP cloud amount during 1983-2009. **c,** Trend in PATMOS-x cloud amount during 1983-2009. **d,** Trend in ensemble mean cloud amount during 1983-2009 from CMIP5 historical simulations with all radiative forcings (ALL). For ISCCP and PATMOS-x, only amount of clouds with optical thickness $\tau > 3.6$ is plotted. Black dots indicate trend statistical significance ($p < 0.05$ two-sided). All trends are relative to the 60°S-60°N mean trend for that pressure interval.

Methods

Satellite Datasets

ISCCP provides values of cloud amount in 7 cloud top pressure intervals and 6 optical thickness intervals (i.e., cloud amount for each of 42 “cloud types”) during July 1983 - December 2009[6]. Total cloud amount is the sum over all intervals. Cloud top pressure is most accurately identified when clouds are nearly opaque at thermal infrared wavelengths. This occurs when cloud optical thickness at visible wavelengths is greater than 3.6. Geostationary satellites are the primary contributors to the ISCCP cloud record. We downloaded ISCCP D1 data from the Atmospheric Science Data Center located at NASA Langley Research Center and applied a correction procedure to remove spurious variability associated with changes in satellite orbits, satellite calibration, and ancillary data[5]. Note that the correction procedure removes any real global mean cloud variability, so all trends presented in this study are with respect to an unknown global mean trend, which could be zero. The present study uses only daytime observations (defined as solar zenith angle < 78°) because visible radiances are required to retrieve cloud optical thickness. We found that trends in total cloud amount retrieved from day and night IR radiances are very similar to trends in total cloud amount retrieved from daytime VIS+IR radiances.

PATMOS-x provides cloud amount in 7 cloud top pressure intervals and 6 optical thickness intervals starting in October 1981[7]. The present study uses data during January 1983 - December 2009 for consistency with ISCCP. Total cloud amount is the sum over all intervals. Polar-orbiting satellites are the only contributors to the PATMOS-x cloud record. We downloaded PATMOS-x Version 5 Level 3 “GEWEX” data from http://cimss.ssec.wisc.edu/patmosx/data and applied a correction procedure to remove spurious variability associated with changes in satellite orbits, satellite calibration, and ancillary data[4]. As for ISCCP, the correction procedure removes any real global mean cloud variability. For consistency over the entire PATMOS-x record, we use products retrieved only from the daytime pass of the “afternoon” satellites.

The passive remote sensing techniques employed by ISCCP and PATMOS-x can have difficulty identifying the occurrence of optically thin cirrus overlying optically thick lower cloud and can underestimate the height of cloud top when cloud particle density is sparse in the upper portion of an optically thick cloud[30,31]. ISCCP suffers more from remote sensing limitations than PATMOS-x since the latter dataset uses more wavelengths and thus has more information available to retrieve cloud properties[7]. The result is a downward bias in reported cloud top height relative to that obtained from active remote sensing techniques, for which only a short record is available. ISCCP correspondingly underestimates the cloud amount in the 50-180 hPa and 180-310 hPa pressure intervals compared to active remote sensing. Despite the bias, a real increase over time in the height of the highest cloud tops will nonetheless be reported by ISCCP as an increase in the amount of cloudiness in the higher elevation pressure interval and decrease in the lower elevation pressure intervals. The bias may produce an underestimate in the magnitude of cloud trends since ISCCP climatological cloud amount is underestimated, but this does not undermine our analysis since we compare the relative spatial patterns of observed and modeled cloud change rather than the absolute magnitudes of observed and modeled cloud change.

Albedo is a useful parameter for our investigation because variability in cloud amount is by far the dominant contributor to variability in albedo outside of ice-covered regions. Variability in cloud optical thickness is a secondary contributor. ERBS albedo values are available for November 1984 through February 1990, but we use the January 1985 - December

1989 climatology for simplicity[13]. We also use measurements only from ERBS because the other two satellites contributing to the Earth Radiation Budget Experiment (NOAA9 and NOAA10) were not available for the entire period. Note that ERBS was in a precessing orbit and sampled the entire diurnal cycle. CERES Energy Balanced And Filled (EBAF) Ed2.8 reflected solar radiation values are available from the morning satellite Terra starting in March 2000 and from the afternoon satellite Aqua starting in July 2002[14]. Since Terra and Aqua are in sun-synchronous orbits CERES EBAF uses geostationary satellites to fill out the diurnal cycle of cloudiness not sampled by Terra and Aqua[15]. To ensure consistent sampling of the diurnal cycle and seasonal cycle, we constructed a climatology for July 2002 - June 2014. We then divided reflected solar radiation by incoming solar radiation at the top of atmosphere to calculate albedo. ERBS data were obtained from a CD-ROM provided by the Atmospheric Science Data Center located at NASA Langley Research Center, and CERES data were obtained from the NASA Langley Research Center CERES ordering tool at (http://ceres.larc.nasa.gov/). Although individually well-calibrated, there is no absolute calibration between ERBS and CERES. To bring them to a common reference point, we multiplied ERBS albedo by a constant factor so that ERBS and CERES had the same climatological annual albedo averaged over 60°S-60°N. This means CERES-ERBS differences are relative to an unknown global mean difference that could be zero.

Version 4 of the MAC-LWP dataset for January 1988 - December 2014 provides a useful complement to measurements of cloud amount and albedo[16]. The MAC-LWP dataset synthesizes passive microwave retrievals from 12 different sensors using the Remote Sensing Systems version-7 ocean algorithm[32]. Liquid water path is the spatially averaged vertically integrated amount of cloud liquid water within a satellite footprint. Cloud-free areas contribute a value of zero to the spatial average within the footprint. Liquid water path increases as clouds become more horizontally extensive (i.e., larger cloud amount). It also increases as clouds become vertically thicker and as cloud water concentration becomes larger. The dataset does not include contributions from cloud ice, and retrievals are available only over open ocean. To provide a similar basis for comparison to the ISCCP, PATMOS-x, and ERBS/CERES datasets, from which global mean variability was removed in the correction and adjustment process, we subtracted 60°S-60°N average liquid water path from the value at each grid box for each month. This has little impact on the spatial distribution of trends.

CMIP5 Simulations

The CMIP5 multi-model dataset provides a large number of global climate model simulations for various forcing scenarios[17]. The historical simulations span ~1850 to 2005 and include time-varying radiative forcings such as greenhouse gases, ozone, anthropogenic and volcanic aerosols, solar output, and land use changes (ALL). We extended the CMIP5 ALL simulations beyond their nominal ending year of 2005 by adding follow-on years through 2009 with radiative forcing from representative concentration pathway 4.5 (or if not available, the historical extended experiment or representative concentration pathway 8.5). Total cloud amount is available from 107 realizations from 33 models, and cloud amount in each vertical layer is available from 76 realizations from 27 models (Extended Data Table 1). We calculated the ensemble mean as a simple average of all available realizations. Some models provided only one realization and other models provided up to 10 realizations for the same external forcing. Natural internal variability across the simulations tends to cancel in the ensemble mean, leaving behind the radiatively forced component of cloud change. The ensemble mean has smaller trend amplitudes than any one realization or the observations due to this reduction of natural internal variability.

A smaller set of CMIP5 models provided additional simulations with external radiative forcing only from anthropogenic greenhouse gases (GHG), only from anthropogenic aerosol (AA), only from ozone (OZ), and only from natural solar variability and volcanic aerosol (NAT) (Extended Data Table 1). A few models included ozone variability in GHG simulations, but we excluded these from our analysis to avoid confusion about forcing factors. Total cloud amount is available from 44 realizations from 14 models for GHG, from 33 realizations from 11 models for AA, from 11 realizations from 3 models for OZ, and from 37 realizations from 10 models for NAT. Cloud amount in each vertical layer is available from 35 realizations from 12 models for GHG, 32 realizations from 11 models for AA, from 1 realizations from 1 model for OZ, and 28 realizations from 8 models for NAT. We did not analyze cloud amount in vertical layers for OZ since only one realization was available.

For many of these models, GHG, AA, OZ, and NAT output was available only until 2005. To maximize the number of realizations, we chose the 1979-2005 interval to calculate trends for GHG and AA since this time period has the same length as the ISCCP and PATMOS-x records. The four-year shift for trend calculation should not matter for the GHG and AA simulations since greenhouse gas and aerosol emissions vary on multidecadal rather than interannual time scales. Timing matters more for OZ and NAT because the former includes stabilization of the ozone hole in the 2000s and the latter includes volcanic eruptions, so we chose only those models providing output for the full 1983-2009 time period. Note that the set of contributing models and numbers of realizations is not identical for the ALL, GHG, AA, OZ, and NAT simulations. We chose to use all available simulations from each forcing scenario because restricting our comparison to only those models and numbers of realizations in common would result in a much smaller sample size.

Most CMIP5 models provided multicentury simulations of preindustrial (PI) conditions with no anthropogenic or natural external radiative forcing as a control case (Extended Data Table 2). Cloud variability in these simulations results only from natural internal variability of the coupled ocean-atmosphere-land system, including El Niño/Southern Oscillation (ENSO). Total cloud amount is available for a total of 15807 years from 27 models, and cloud amount in each vertical layer is available for a total of 7311 years from 13 models.

Output from CMIP5 simulations was downloaded from the Earth System Grid Federation (ESGF). To provide a similar basis for comparison to the ISCCP, PATMOS-x, and ERBS/CERES datasets, from which global mean variability was removed in the correction and adjustment process, we subtracted 60°S-60°N ocean average cloud amount from the value at each ocean grid box for each month and we subtracted 60°S-60°N land average cloud amount from the value at each land grid box. With the exception of cloud amount in the 50-180 hPa interval, this has little impact on the spatial distribution of trends. For zonally-averaged cloud amount in each vertical layer, we subtracted the 60°S-60°N average.

Since the CMIP5 models do not routinely report amount of cloudiness in various optical thickness intervals, we could not limit our analysis of modeled clouds in Fig. 3 to only those with optical thickness greater than 3.6. Cloud amount from the satellite records also differs from standard cloud amount output from CMIP5 models in that the former do not detect clouds with optical thickness less than about 0.3 whereas the latter report the amount of all clouds, even very optically thin ones. Another difference is that CMIP5 models report actual cloud amount at each model layer, not cloud amount unobscured by higher clouds as do the ISCCP and PATMOS-x satellite datasets. For a closer comparison to observations, a few CMIP5 models incorporated the Cloud Feedback Model Intercomparison Project (CFMIP) Observation Simulator Package (COSP)[33]. This software produced model cloud output according to how it would be detected through the limitations of satellite retrieval, most often ISCCP. Since it is computationally expensive, COSP cloud output is available only for 13 ALL realizations from 7 models (Extended Data Table 1). We use standard model cloud output in order to have a larger sample size but obtain similar but noisier results if we use COSP cloud output from an ISCCP satellite simulator (Extended Data Fig. 8).

Data Analysis

ISCCP, PATMOS-x, and ERBS data on a 2.5°×2.5° latitude-longitude grid and CERES and MAC-LWP data on a 1°×1° grid were spatially averaged to a common 5°×5° grid. Output from CMIP5 models on a variety of grid sizes were bilinearly interpolated to a 5°×5° grid. We linearly interpolated cloud amount from model layers to a common vertical grid with regular 50 hPa spacing in pressure. To display modeled cloud trends in the figures, we linearly interpolated trends from the 50 hPa regular grid to the midpoints of the 7 pressure intervals used by the satellite datasets. All calculations are performed on anomalies from the long-term mean. In all cases of spatial averaging and spatial correlation, grid box values were weighted by the cosine of the grid box center latitude to account for the variation of grid box area with latitude. We restrict our analysis to latitudes equatorward of 60° because passive retrieval of cloud properties by satellite is difficult over bright and cold surfaces, and no visible retrievals can be made during polar night.

We use least-squares linear trends or the average difference between two time periods as convenient means of summarizing change over time. Two-sided p-values for the trends are determined using a conventional Student's t-test with an effective sample size that takes temporal autocorrelation into account.

For simplicity of comparison with modeled total cloud amount trends in calculating correlations in Table 1, we averaged cloud/albedo changes from all cloud amount and albedo datasets together before comparing to the ensemble mean total cloud amount trends from the CMIP5 ALL, GHG, AA, OZ, NAT, and PI simulations. Since cloud amount and albedo have different physical units, we standardized the grid box changes before averaging. Specifically, we divided each ISCCP grid box cloud amount trend by the standard deviation of all ISCCP grid box cloud amount trends, each PATMOS-x grid box cloud trend by the standard deviation of all PATMOS-x grid box cloud amount trends, and each grid box albedo change by the standard deviation of all grid box albedo changes. For simplicity of comparison with modeled cloud amount trends in 7 pressure intervals, we averaged cloud trends from ISCCP and PATMOS-x datasets together.

Our null hypothesis is that the observed cloud changes result purely from natural internal variability. If so, there should be no systematic relationship between the spatial pattern of cloud trends generated by natural internal variability and the spatial pattern of cloud trends generated by external radiative forcing. The former is represented by individual PI simulations, each with different realizations of natural internal variability, and the latter is represented by the ensemble mean of simulations with external radiative forcing, in which natural variability has been largely averaged out. The suitability of this null hypothesis can be demonstrated by calculating the distribution of spatial correlation coefficients (Pearson's r) between the pattern of cloud trends from the ensemble mean of forced simulations (ALL, GHG, or NAT) and the pattern of cloud trends from time periods of similar length obtained from PI control simulations. We build up each null distribution by calculating cloud trends and spatial correlation values during a rolling 27-year period (i.e., years 1-27, years 2-28, years 3-29, etc.) through the PI control simulation for each model. Extended Data Fig. 3 displays the frequency distributions of the calculated correlation values. There are 15104 time periods for total cloud amount and 6973 time periods for cloud amount in vertical layers. The mean and median correlation values of the null distributions are zero, as expected.

Our alternative hypothesis is that external radiative forcing was a contributing factor in producing the observed cloud trends. If so, we expect a positive spatial correlation between the observed trend pattern and the trend pattern from the ensemble mean of simulations with external radiative forcing (values shown as vertical lines in Extended Data Fig. 3). The *p*-value for a particular spatial correlation value r is simply the fraction of correlation values from the PI control simulations with values more positive than r (i.e., the fraction of area under the frequency distribution to the right of the vertical line). For simplicity, we calculate *p*-values with respect to a null distribution built from spatial correlation values for cloud trends from single time periods. Another option is to build a null distribution from spatial correlation values for cloud trends from ensemble means of multiple, randomly-selected time periods. Our results are the same for either approach.

For corroboration of *p*-values calculated with respect to cloud trend patterns from the PI control simulations, we additionally computed one-sided *p*-values using a conventional Student's *t*-test for statistical significance of Pearson's r. In this case, a critical parameter is the effective number of spatial degrees of freedom[34]. We determined that there are 51 spatial degrees of freedom between 60°S and 60°N for observed total cloud amount in grid boxes. Simplistically considered, this corresponds to a set of boxes slightly larger than those outlined by the latitude-longitude grid lines in Fig. 1 if apportioned equally. However, remote teleconnections contribute to reduced spatial degrees of freedom in addition to local spatial coherence. Zonal means have substantially fewer degrees of freedom (8 for total cloud amount and 7 for cloud amount in the 50-180 hPa and 180-310 hPa pressure intervals). This corresponds to about 15° spacing in latitude. *P*-values obtained from formal tests are in some cases substantially larger than those obtained from the PI control simulations (Table 1 and Extended Data Fig. 3), suggesting that the actual number of effective spatial degrees of freedom may be larger than that indicated by the method we used[34].

ENSO-like Variability

The dominant source of multiyear natural variability in the climate system is the El Niño/Southern Oscillation (ENSO) phenomenon. Variability occurring at interdecadal time scales, especially over the Pacific Basin, exhibits a pattern similar to that of ENSO[35]. We investigated whether the observed cloud changes are a manifestation of ENSO-like variability by calculating the correlation of the spatial pattern of cloud trends with the spatial pattern of the difference between observed La Niña composite cloud anomalies and El Niño composite cloud anomalies (figure not shown due to space limitations). The correlation between the observed La Niña - El Niño pattern and the observed trend pattern is only 0.13, and the spatial correlation between the observed La Niña - El Niño pattern and the ensemble mean ALL trend pattern is only 0.14. Considering that the spatial correlation between the observed trend pattern and the ensemble mean ALL trend pattern is 0.39 (Table 1), we think ENSO-like variability cannot be a major contributor to the global pattern of cloud change between the 1980s and the 2000s.

References

30. Mace, G. G., & Wrenn, F. J., Evaluation of the hydrometeor layers in the East and West Pacific within ISCCP cloud-top pressure-optical depth bins using merged CloudSat and CALIPSO data, *J. Climate*, **26**, 9429-9444 (2013).

31. Sherwood, S. C., Chae, J.-H., Minnis,P., & M. McGill, M., Underestimation of deep convective cloud tops by thermal imagery, *Geophys. Res. Lett.*, **31**, L11102, (2004).

32. Hilburn, K. A., & Wentz, F. J. Intercalibrated passive microwave rain products from the unified microwave ocean retrieval algorithm (UMORA), *J. Appl. Meteor. Climatol.*, **47**, 778-794 (2008).

33. Bodas-Salcedo, A. *et al.* 2011: COSP: Satellite simulation software for model assessment. *Bull. Amer. Meteor. Soc.*, 92, 1023–1043 (2011).

34. Bretherton, C. S., Widmann, M., Dymnikov, V. P., Wallace, J. M., & Bladé, I. The effective number of *spatial* degrees of freedom of a time-varying field, *J. Climate*, **12**, 1990-2009 (1999).

35. Zhang, Y., Wallace, J. M., & D. S. Battisti, ENSO-like interdecadal variability: 1900–93, *J. Climate*, **10**, 1004–1020 (1997).

Extended Data Table 1

CMIP5 models and number of simulations used for each forcing experiment

Model	ALL		GHG	AA	OZ	NAT
	Standard	COSP				
ACCESS1-0	(1)					
ACCESS1-3	(1)					
BCC-CSM1-1	3		1			1
BCC-CSM1-1-m	3					
BNU-ESM	1		1			
CanESM2	5	1	5	5		5
CCSM4	6		3	3		
CESM1-CAM5	3					
CESM1-CAM5-1-FV2	1		2	2		
CESM1-WACCM	3					
CMCC-CM	1					
CMCC-CMS	1					
CNRM-CM5	(10)		(5)			(5)
CSIRO-Mk3-6-0	10		5	5		5
EC-EARTH	(5)					
FGOALS-g2			1	2	1	
GFDL-CM3	1			3		
GFDL-ESM2G	1					
GFDL-ESM2M	1		1	1		
GISS-E2-H	5		5	5	(5)	5
GISS-E2-H-CC	1					
GISS-E2-R	5		5	5	(5)	5
GISS-E2-R-CC	1					
HadCM3	(10)					
HadGEM2-ES	(4)	1	(4)			(4)
IPSL-CM5A-LR	4		3	1		3
IPSL-CM5A-MR	1		3			3
MIROC5	5	5				
MIROC-ESM	1	3				
MIROC-ESM-CHEM	1	1				
MPI-ESM-LR	3	1				
MPI-ESM-MR	3					
MRI-CGCM3	3	1				
NorESM1-M	3			1		1

Parentheses indicate unavailability of vertical distribution of cloud amount

Extended Data Table 2

CMIP5 models and number of years in each preindustrial control simulation

Model	Total Cloud Amount	Layer Cloud Amount
ACCESS1-0	500	
ACCESS1-3	500	
BCC-CSM1-1	500	500
BCC-CSM1-1-m	400	400
BNU-ESM	559	559
CanESM2	996	796
CCSM4	1000	1000
CESM1-CAM5	319	
CESM1-WACCM	200	
CNRM-CM5	850	
CSIRO-Mk3-6-0	500	
FGOALS-g2	700	
GFDL-CM3	500	500
GFDL-ESM2G	500	500
GFDL-ESM2M	500	500
GISS-E2-H	540	
GISS-E2-R	550	
HadGEM2-ES	337	
IPSL-CM5A-LR	1000	
IPSL-CM5A-MR	300	
MIROC5	670	670
MIROC-ESM	630	630
MIROC-ESM-CHEM	255	255
MPI-ESM-LR	1000	
MPI-ESM-MR	1000	
MRI-CGCM3	500	500
NorESM1-M	501	501

Extended Data Figure Legends

Extended Data Figure 1 | Change in observed liquid water path during 1988-2014. **a,** Linear trend in MAC-LWP liquid water path during Jan 1988-Dec 2014. **b,** Zonal mean climatology (red) and trend (black) in MAC-LWP liquid water path during Jan 1988-Dec 2014. Circles indicate trend statistical significance ($p < 0.05$ two-sided). All trends are relative to the 60°S-60°N mean trend.

Extended Data Figure 2 | Change in observed cloud amount and albedo between Jan 1985-Dec 1989 and Jan 2003-Dec 2009. a, ISCCP total cloud amount. **b,** PATMOS-x total cloud amount. **c,** ERBS/CERES albedo. Black dots indicate agreement among all three satellite records on sign of change in **a**, **b**, and **c**. All changes are relative to the 60°S-60°N mean change.

Extended Data Figure 3 | Correlation between forced simulated, unforced simulated, and observed cloud trend patterns. Frequency distribution of correlation between cloud trend patterns from multiple individual unforced CMIP5 preindustrial (PI) simulations and the ensemble mean of CMIP5 historical simulations with all radiative forcings (ALL, black), only greenhouse radiative forcings (GHG, red), and only natural radiative forcings (NAT, blue) for 27-year trends. **a,** Grid box total cloud amount. **b,** Zonal mean total cloud amount. **c,** Zonal mean cloud amount in the 50-180 hPa and 180-320 hPa intervals. Vertical lines indicate the correlation coefficient between the pattern of observed cloud trends and the pattern of ensemble mean ALL, GHG, or NAT cloud trends during 1983-2009. The total area under each frequency distribution is equal to unity, and the area to the right of the vertical line indicates the fraction of PI simulations that are more positively correlated than the observations with the ensemble mean ALL, GHG, or NAT cloud trend patterns (listed as *p*-values in Table 1).

Extended Data Figure 4 | Absolute change in simulated cloud amount during 1983-2009. **a,** Linear trend in ensemble mean total cloud amount during 1983-2009 from CMIP5 historical simulations with all radiative forcings (ALL). **b,** Zonal mean climatology (red) and trend (black) in ensemble mean total cloud amount during 1983-2009 from ALL simulations. **c,** Zonal mean trend in ensemble mean cloud amount during 1983-2009 in 7 pressure intervals from ALL simulations. Black dots and circles indicate trend statistical significance ($p < 0.05$ two-sided), and bars indicate interquartile range of individual simulations. Unlike Figs. 1c, 2d, and 3d, trends are not relative to the 60°S-60°N mean trend.

Extended Data Figure 5 | Change in simulated cloud amount between the 1980s and 2000s for different types of forcing. Linear trend in ensemble mean total cloud amount from CMIP5 simulations and locations where the majority of observational datasets and majority of simulations show increasing (cyan) or decreasing (orange) cloud amount or albedo. **a** and **b,** Only greenhouse gas (GHG) forcing during 1979-2005. **c** and **d,** Only anthropogenic aerosol (AA) forcing during 1979-2005. **e** and **f,** Only ozone (OZ) forcing during 1983-2009. **g** and **h,** Only natural (NAT) forcing during 1983-2009. Black dots indicate trend statistical significance ($p < 0.05$ two-sided). All trends are relative to the 60°S-60°N mean trend.

Extended Data Figure 6 | Zonal mean change in simulated cloud amount between the 1980s and 2000s for different types of forcing. Climatology is red and linear trend is black for ensemble mean total cloud amount from CMIP5 simulations. **a,** Only greenhouse gas (GHG) forcing during 1979-2005. **b,** Only anthropogenic aerosol (AA) forcing during 1979-2005. **c,** Only ozone (OZ) forcing during 1983-2009. **d,** Only natural (NAT) forcing during 1983-2009. Circles indicate trend statistical significance ($p < 0.05$ two-sided) and bars indicate interquartile range of individual simulations. All trends are relative to the 60°S-60°N mean trend.

Extended Data Figure 7 | Zonal mean change in simulated cloud amount between the 1980s and 2000s in 7 pressure intervals for different types of forcing. Linear trend for ensemble mean cloud amount from CMIP5 simulations. **a,** Only greenhouse gas (GHG) forcing during 1979-2005. **b,** Only anthropogenic aerosol (AA) forcing during 1979-2005. **c,** Only natural (NAT) forcing during 1983-2009. Black dots indicate trend statistical significance ($p < 0.05$ two-sided). All trends are relative to the 60°S-60°N mean trend for that pressure interval.

Extended Data Figure 8 | Change in simulated cloud amount during 1983-2009 from the CFMIP Observation Simulator Package (COSP). a, Linear trend in ensemble mean total cloud amount during 1983-2009 from CMIP5 historical simulations with all radiative forcings (ALL). **b,** Zonal mean climatology (red) and trend (black) in ensemble mean total cloud amount during 1983-2009 from ALL simulations. **c,** Zonal mean trend in ensemble mean cloud amount during 1983-2009 in 7 pressure intervals from ALL simulations. Black dots and circles indicate trend statistical significance ($p < 0.05$ two-sided), and bars indicate interquartile range of individual simulations. All trends relative to the 60°S-60°N mean trend.

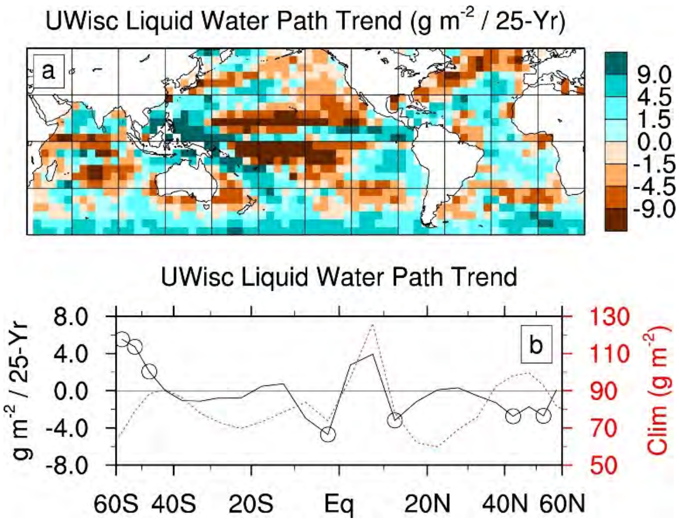

Extended Data Figure 1 | Change in observed liquid water path during 1988-2014. **a,** Linear trend in MAC-LWP liquid water path during Jan 1988-Dec 2014. **b,** Zonal mean climatology (red) and trend (black) in MAC-LWP liquid water path during Jan 1988-Dec 2014. Circles indicate trend statistical significance ($p < 0.05$ two-sided). All trends are relative to the 60°S-60°N mean trend.

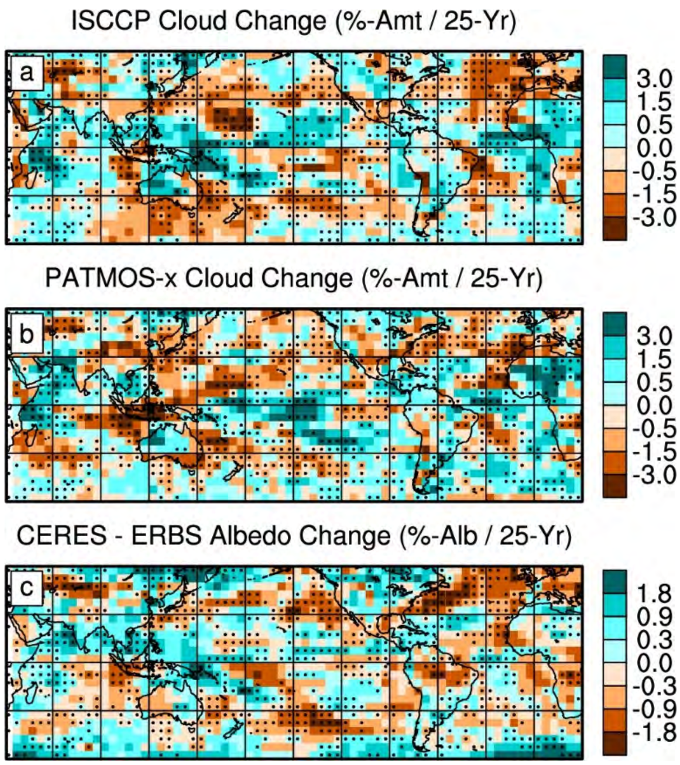

Extended Data Figure 2 | Change in observed cloud amount and albedo between Jan 1985-Dec 1989 and Jan 2003-Dec 2009. a, ISCCP total cloud amount. **b,** PATMOS-x total cloud amount. **c,** ERBS/CERES albedo. Black dots indicate agreement among all three satellite records on sign of change in **a**, **b**, and **c**. All changes are relative to the 60°S-60°N mean change.

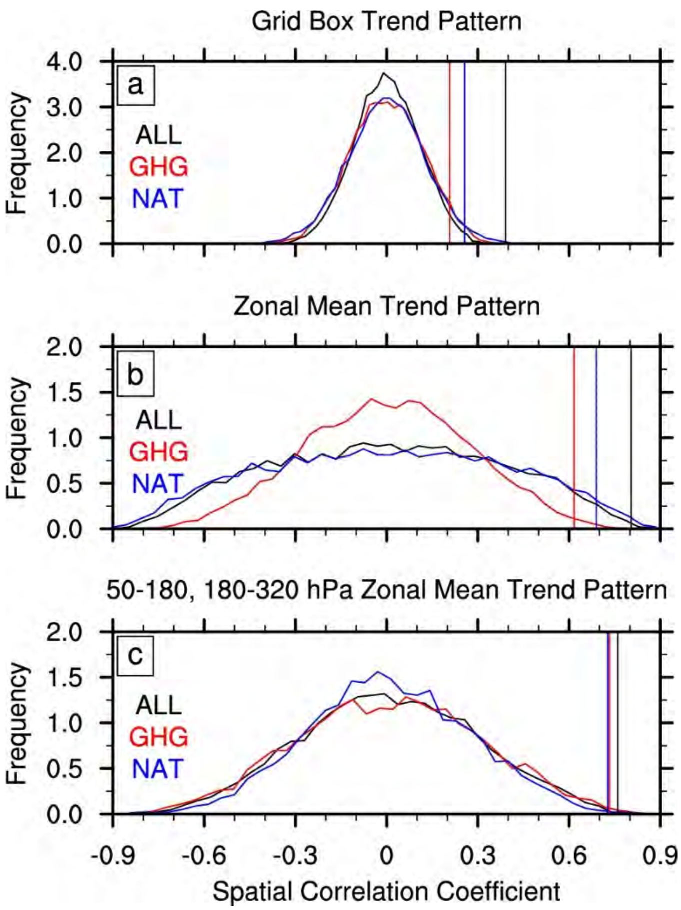

Extended Data Figure 3 | Correlation between forced simulated, unforced simulated, and observed cloud trend patterns. Frequency distribution of correlation between cloud trend patterns from multiple individual unforced CMIP5 preindustrial (PI) simulations and the ensemble mean of CMIP5 historical simulations with all radiative forcings (ALL, black), only greenhouse radiative forcings (GHG, red), and only natural radiative forcings (NAT, blue) for 27-year trends. **a,** Grid box total cloud amount. **b,** Zonal mean total cloud amount. **c,** Zonal mean cloud amount in the 50-180 hPa and 180-320 hPa intervals. Vertical lines indicate the correlation coefficient between the pattern of observed cloud trends and the pattern of ensemble mean ALL, GHG, or NAT cloud trends during 1983-2009. The total area under each frequency distribution is equal to unity, and the area to the right of the vertical line indicates the fraction of PI simulations that are more positively correlated than the observations with the ensemble mean ALL, GHG, or NAT cloud trend patterns (listed as *p*-values in Table 1).

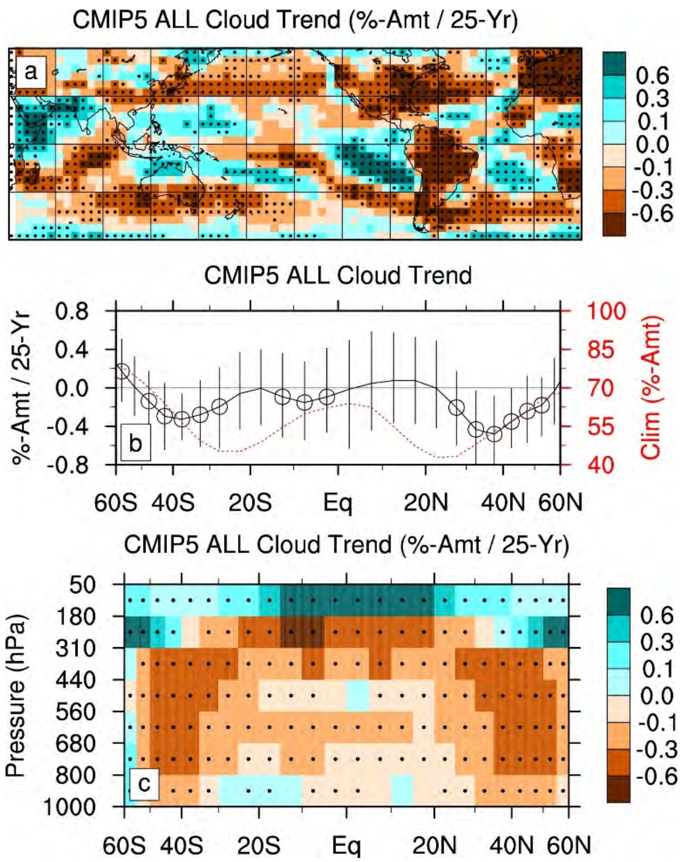

Extended Data Figure 4 | Absolute change in simulated cloud amount during 1983-2009. **a,** Linear trend in ensemble mean total cloud amount during 1983-2009 from CMIP5 historical simulations with all radiative forcings (ALL). **b,** Zonal mean climatology (red) and trend (black) in ensemble mean total cloud amount during 1983-2009 from ALL simulations. **c,** Zonal mean trend in ensemble mean cloud amount during 1983-2009 in 7 pressure intervals from ALL simulations. Black dots and circles indicate trend statistical significance ($p < 0.05$ two-sided), and bars indicate interquartile range of individual simulations. Unlike Figs. 1c, 2d, and 3d, trends are not relative to the 60°S-60°N mean trend.

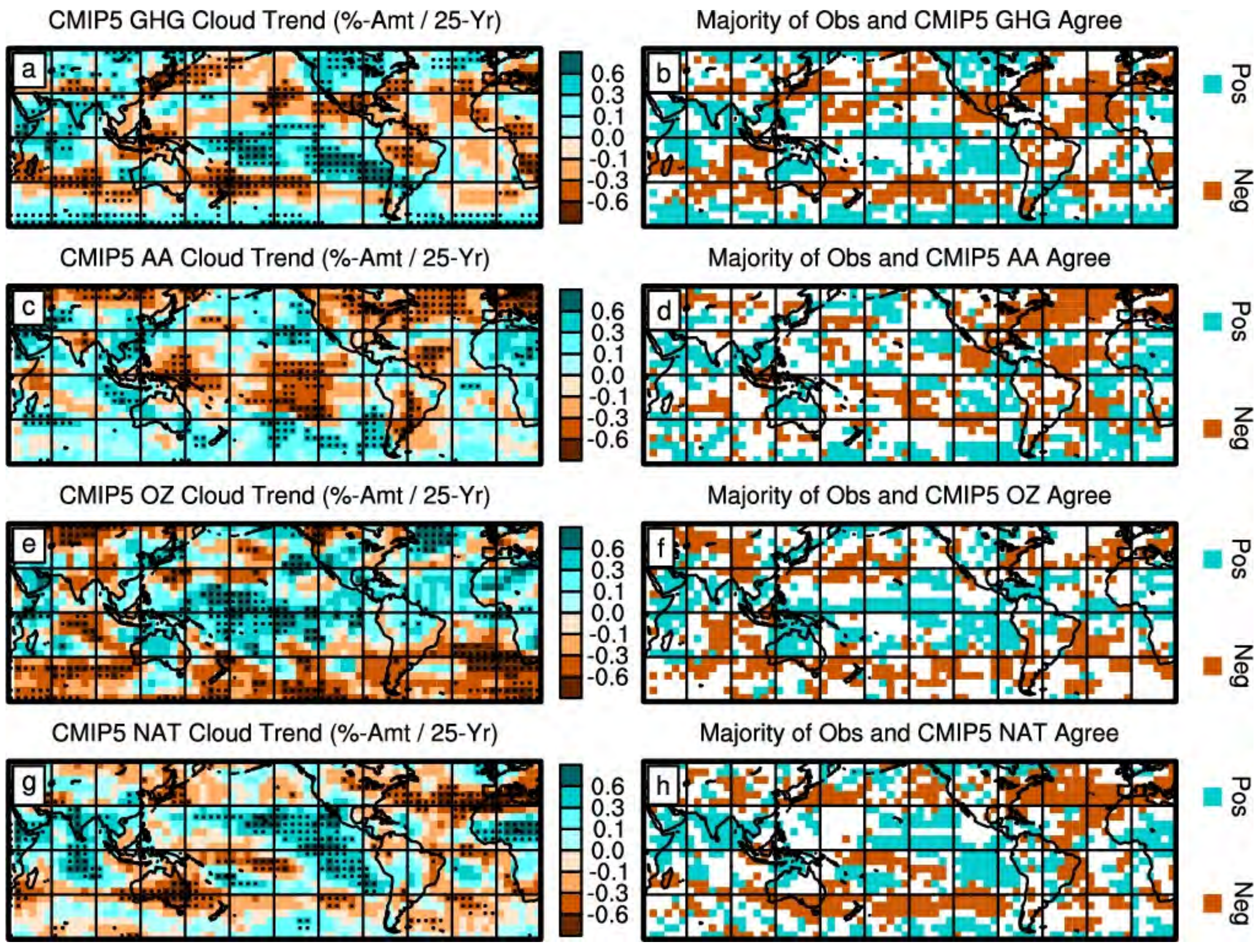

Extended Data Figure 5 | Change in simulated cloud amount between the 1980s and 2000s for different types of forcing. Linear trend in ensemble mean total cloud amount from CMIP5 simulations and locations where the majority of observational datasets and majority of simulations show increasing (cyan) or decreasing (orange) cloud amount or albedo. **a** and **b,** Only greenhouse gas (GHG) forcing during 1979-2005. **c** and **d,** Only anthropogenic aerosol (AA) forcing during 1979-2005. **e** and **f,** Only ozone (OZ) forcing during 1983-2009. **g** and **h,** Only natural (NAT) forcing during 1983-2009. Black dots indicate trend statistical significance ($p < 0.05$ two-sided). All trends are relative to the 60°S-60°N mean trend.

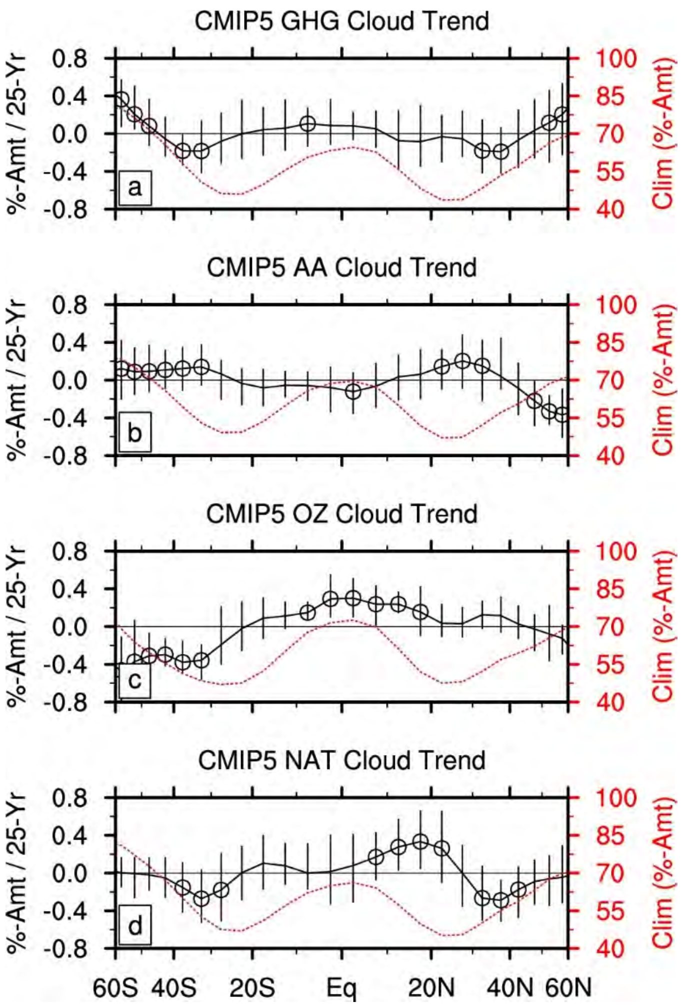

Extended Data Figure 6 | Zonal mean change in simulated cloud amount between the 1980s and 2000s for different types of forcing. Climatology is red and linear trend is black for ensemble mean total cloud amount from CMIP5 simulations. **a,** Only greenhouse gas (GHG) forcing during 1979-2005. **b,** Only anthropogenic aerosol (AA) forcing during 1979-2005. **c,** Only ozone (OZ) forcing during 1983-2009. **d,** Only natural (NAT) forcing during 1983-2009. Circles indicate trend statistical significance ($p < 0.05$ two-sided) and bars indicate interquartile range of individual simulations. All trends are relative to the 60°S-60°N mean trend.

.

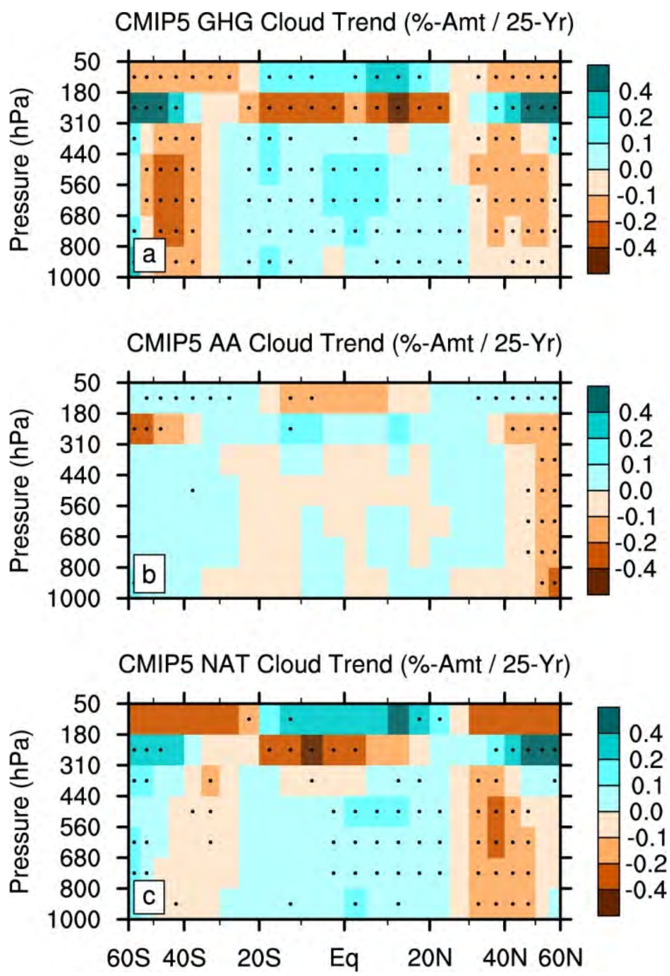

Extended Data Figure 7 | Zonal mean change in simulated cloud amount between the 1980s and 2000s in 7 pressure intervals for different types of forcing. Linear trend for ensemble mean cloud amount from CMIP5 simulations. **a,** Only greenhouse gas (GHG) forcing during 1979-2005. **b,** Only anthropogenic aerosol (AA) forcing during 1979-2005. **c,** Only natural (NAT) forcing during 1983-2009. Black dots indicate trend statistical significance ($p < 0.05$ two-sided). All trends are relative to the 60°S-60°N mean trend for that pressure interval.

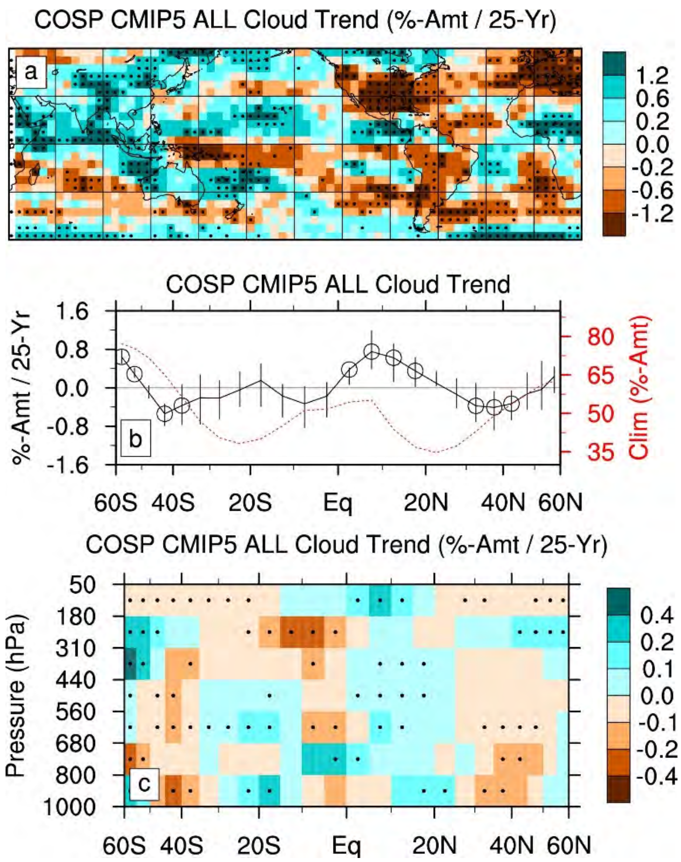

Extended Data Figure 8 | Change in simulated cloud amount during 1983-2009 from the CFMIP Observation Simulator Package (COSP). a, Linear trend in ensemble mean total cloud amount during 1983-2009 from CMIP5 historical simulations with all radiative forcings (ALL). **b,** Zonal mean climatology (red) and trend (black) in ensemble mean total cloud amount during 1983-2009 from ALL simulations. **c,** Zonal mean trend in ensemble mean cloud amount during 1983-2009 in 7 pressure intervals from ALL simulations. Black dots and circles indicate trend statistical significance ($p < 0.05$ two-sided), and bars indicate interquartile range of individual simulations. All trends relative to the 60°S-60°N mean trend.